Numerical investigation of tilt angle effect on a Direct Steam Generation solar receiver

Israël Aguilera-Cortes, Adrien Toutant, Samuel Mer

Solar Energy 287 (2025) 113215

Contents lists available at ScienceDirect

Solar Energy

journal homepage: www.elsevier.com/locate/solener

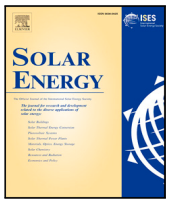

Numerical investigation of tilt angle effect on a Direct Steam Generation solar receiver

Israël Aguilera-Cortes *, Adrien Toutant, Samuel Mer

PROMES Laboratory, CNRS - Université de Perpignan Via Domitia, Perpignan, France

ARTICLE INFO

Keywords:
Direct Steam Generation
CFD modeling
Conjugate heat transfer
Boiling flow

ABSTRACT

Direct steam generation (DSG), which is currently gaining renewed interest in concentrated solar power technologies, offers several advantages, such as reducing the number of components in the plant and lowering operating costs by replacing conventional heat transfer fluids — usually synthetic oils or molten salts — with water. However, it also introduces certain complexities due to the two-phase flow in the receiver. In horizontal receivers, gravity tends to separate the two phases, generating a stratified flow regime. In this regime, steam transfers heat less efficiently, causing the upper part of the receiver to overheat and creating significant temperature gradients within the receiver. These gradients can lead to fatigue and reduce the lifespan of components. Therefore, predicting flow regimes is crucial for the design and operation of solar power plants. In pursuit of this objective, we are developing a 3D transient modeling tool using the NEPTUNE_CFD and Syrthes software to account for the two-phase flow dynamic and coupled heat transfers within the receiver. Simulations, based on a 67 m long receiver module from the eLLO plant, study the influence of the receiver's inclination and the distribution of concentrated solar flux on the receiver's performance. The results show that flux distribution mainly affects the temperature distribution in the solid but does not impact steam production. Flow regimes are strongly influenced by the receiver's inclination. Downward configurations promote steam production at the cost of greater temperature gradients.

1. Introduction

Concentrated Solar Power (CSP) is an emerging technology that is positioning itself as a viable alternative to conventional energy generation technologies [1]. The fundamental principle of this technology lies in concentrating solar radiation at a focal point (as in tower or Dish Stirling plants) or along a focal line (as in parabolic trough or Fresnel plants). This focused concentration of electromagnetic radiation enables the working fluid to reach high temperatures up to 560 °C for molten salts. Inside the receiver, the heat transfer fluid (HTF) is responsible for absorbing the radiation energy concentrated by the mirrors. This energy now held in the HTF can be used for different purposes, such as the production of electricity, the salt-water desalinization or the production of steam for industrial processes. When the HTF is water, steam is generated directly in the receiver, leading to the so-called Direct Steam Generation (DSG) technology. In this process, pressurized subcooled water is injected into the receiver, where it first heats up to the saturation temperature and then evaporates, creating a mixed flow of water and steam. The steam produced can be either used in a steam turbine to produce electricity or directly in steam driven industrial processes (*e.g.:* paper mills, food processing, oil extraction…). The DSG technology presents several significant advantages:

- **Simplicity and efficiency:** Eliminating the heat transfer fluid simplifies the system and reduces the number of heat exchangers (preheater, boiler, and superheater). This increases the overall efficiency of the plant [2] due to the reduction in the number of components.
- **Cost reduction:** Eliminating the working fluid reduces acquisition, maintenance, and operational costs, making the plant more cost-effective in the long term [3].
- **Reduced environmental impact:** Simplifying the design and reducing the number of components decreases the associated carbon footprint. It also reduces plant waste, enhancing social acceptance.

The process of generating steam directly in the receiver involves the coexistence of both liquid and steam phases during evaporation. Due to differences in densities and buoyancy forces, the steam phase tends to move upward toward the top of the receiver. The presence of these two phases in a horizontal receiver generates various flow patterns, which depend on the system's operational parameters, such as mass flow rate, heat flux, or tilt. Studying these flow patterns is crucial, as

* Corresponding author.
E-mail address: israel.aguilera-cortes@cnrs.fr (I. Aguilera-Cortes).

https://doi.org/10.1016/j.solener.2024.113215
Received 25 October 2024; Received in revised form 6 December 2024; Accepted 18 December 2024

Nomenclature

Abbreviations

CG	Continuous gas
CL	Continuous liquid
CSP	Concentrated solar power
DG	Dispersed gas
DISS	Direct solar steam
DSG	Direct steam generation
HTF	Heat transfer fluid
LFC	Linear fresnel concentrator
PTC	Parabolic-trough collector
RANS	Reynolds-averaged Navier–Stokes equations
RMS	Root mean square
SIMPLE	Semi-implicit method for pressure linked equations

Greek symbols

α	Void fraction [-]
δ	Kronecker symbol [-]
κ	Interface curvature [m^{-1}]
λ	Wall conductivity [W m^{-1} K^{-1}]
μ	Dynamic viscosity [kg m^{1} s^{-1}]
ρ	Density [kg m^{-3}]
σ	Surface tension [N m^{-1}]
τ	Characteristic time [s]
Θ	Circumferential angle [°]
θ	Tilt angle [°]
ϵ	Turbulent kinetic energy dissipation [m^2 s^{-3}]

Roman symbols

$\ddot{x}$	Dynamic steam quality [-]
$\dot{m}$	Mass flow rate [kg s^{-1}]
$\dot{x}$	Steam quality [-]
c_p	Thermal capacity [J K^{-1} kg^{-1}]
D	Diameter [m]
E^{int}	Interfacial thermal transfer [W m^{-3}]
G	Mass flux [kg m^{-2} s^{-1}]
g	Gravity [m s^{-2}]
H	Enthalpy [J kg^{-1}]
h	Heat transfer coefficient [W m^{-2} K^{-1}]
I	Momentum transfer [N m^{-3}]
L	Length [m]
P	Pressure [Pa]
Q	Conductive flow [W m^{-2}]
Re	Reynolds number [-]
St	Stanton number [-]
T	Temperature [K]
u	Velocity [m s^{-1}]

Subscripts

b	Bubble
crl	Critical
c	Convective
d	Detachment
e	Evaporation
i, j	Spacial direction
in, out	Inlet, outlet
l, s, v	Liquid, solid, vapor
lat	Latent
p, k	Phase p, k
q	Quenching
sat	Saturation
w	Wall

Subscripts

AM	Added mass
D	Drag
F	Friction
int	Interface
L	Lift
nuc	Nucleation
P	Penalty force
T	Turbulent

the heat transfer coefficient between the receiver tube and the fluid varies significantly with the flow pattern [4–6]. Numerous flow regime maps have been developed for two-phase flow in horizontal pipes, with and without phase change. Baker [7] proposed a map for flow in small-diameter pipes using various fluids adiabatic flow data. In its representation, the flow pattern depends on the mass flow rates of each phases, ponderated by non-dimensional parameters taking into account physical properties of the fluids (density, viscosity, surface tension). Mandhane et al. [8] studied two-phase flow in small-diameter pipe adiabatic air–water flows and constructed a map based on gas and liquid surface velocities. This type of map is now the most widely used. Taitel and Dukler [4] developed a theoretical and mechanistic flow regime map, which remains widely used today. However, the flow regime maps available in the literature are not fully adapted to the current operating conditions of modern plants. Specifically, the work by [4,7,8] focuses on horizontal air–water flows without accounting for heat and mass transfer. In a DSG receiver, the vapor mass flow rate is null at the inlet and grows wih the streamwise direction owing to boiling. The previously introduced maps do not account for this phenomenon and require the *a priori* knowledge of the *gas* mass flow rates. Horizontal boiling flow maps do exist in the literature, one can refer to the work of [5,6], however, those maps are limited to small-diameter tubes (where confinement plays a dominant role) and refrigerants (which have a much lower latent heat compared to water).

The modeling and simulation of direct steam generation (DSG) have extensively employed two principal approaches: the homogeneous equilibrium model (HEM) and the two-fluid model (TFM), each offering distinct advantages and limitations. HEM, which assumes thermal and mechanical equilibrium between phases, has been successfully applied in scenarios with homogeneous flow conditions, such as the recirculation operation mode, where its simplicity and low computational cost make it highly effective. Notable examples include its use in thermohydraulic studies of parabolic collectors integrated with thermal energy storage systems, as demonstrated in the DISS project, and its implementation in simplified modeling tools such as TRNSYS [2], RELAP5 HEM [9] or in-house codes made by several institutions such as University of New South Wales [10], DLR [11,12] or PSA [13,14]. However, HEM lacks precision in representing complex or transient flows.

Conversely, TFM offers a significant advancement by independently modeling mass, momentum, and energy conservation equations for each phase [15], enabling a more accurate representation of phenomena such as bifurcated flow patterns and thermohydraulic instabilities. This approach has been employed in advanced simulations using tools such as NEPTUNE CFD, which incorporates interfacial interaction models to enhance the prediction of behavior at the evaporation endpoint

and superheating sections. These capabilities are particularly valuable for addressing challenges related to solar radiation transients and flow pattern transitions, which are critical in DSG applications. Similarly, SYRTHES complements this approach by focusing on transient heat transfer between fluids and solids, facilitating the design and evaluation of thermal energy storage systems in DSG receivers.

Thermal stress in linear solar concentrators is also a significant area of research due to how concentrated radiation affects the receiver. In linear Fresnel concentrators (LFC), only about half of the receiver is exposed to concentrated radiation. In Direct Steam Generation (DSG) systems, thermal stress becomes even more critical for two main reasons. Firstly, higher operating pressures require thicker tube walls, which intensify temperature gradients within the tube [16,17]. On the other hand, the stratification of the two phases increase these gradients because the steam at the top of the receiver evacuates the heat inefficiently compare to the water at the bottom. As a result, uneven heat transfer within the tube increases thermal load, causing thermal bending that may damage the absorber tube.

It is evident that the flow regimes in the receiver are a crucial point when designing a power plant. The topography of the solar field must also be taken into account, as the phase distribution changes with the slope of the receiver. The effect of tilt has been previously studied experimentally at the DISS experimental facility at the Plataforma Solar de Almería [18,19], showing that inclination of the absorber pipe reduced the stratified region. However such experimental studies have their limitations [20,21], as temperature sensors measure point temperature while a temperature field is required to precisely assess the thermal gradient generating the thermal stress. Numerical simulations appears to be an interesting tool to study these phenomena. Previous numerical studies focusing on horizontal receivers operating with DSG technology are reported in the literature. Those are mainly dedicated to PTC and non-Fresnel receivers [22,23]. However, these have been carried out using stationary numerical method, while the nature of the flow pattern inside the receivers is deeply transient.

This study aims to investigate the influence of the tilt angle on a receiver with a similar geometry of a real commercial plant (eLLO). Both positive and negative tilt angles are considered, as well as the influence of boundary conditions and the application of homogeneous and non-homogeneous heat flux on the external surface of the receiver. The study approach involves performing Computational Fluid Dynamics (CFD) simulations considering conjugated heat transfer in the solid domain of the receiver. The software used for these simulations are NEPTUNE_CFD and SYRTHES, which were both developed by a french consortium of industrial nuclear energy actors, led by EDF. The numerical methods involved in those two solvers are fully transient and will allow the evaluation of temporal fluctuations of the parameters of interest.

The paper is organized as follows. Section 2 presents the case study of the eLLO power plant. In Section 3 the different equations and hypotheses of the numerical method used are detailed. A validation by comparison with various cases of the literature is subsequently presented in Section 4 along with a mesh sensitivity analysis. Section 5 presents the simulated calculation configurations and the simulation procedure. The results obtained are presented and analyzed in Section 6. Finally, Section 7 summarizes the main findings and draw some prospects for this work.

2. Case study: eLLO plant

The eLLO plant, a 9 MW Fresnel-type facility located in Cerdanya in southern France, uses DSG technology. It is the first and only commercial plant of its kind in the world that produces and injects electricity into the grid. The power plant includes a large thermal storage system consisting of 9 Ruth accumulators, each one with a capacity of 120 m^3, connected in parallel [25]. It enables an electrical production delayed from the solar resource. Such construction is in accordance with the findings of [26] who observed that Fresnel concentrators are generally preferred for DSG electricity production. Table 1 presents the main features of the power plant. One particular feature of this plant is that it is built on sloped terrain that was not previously leveled, resulting in receivers inclined both in the direction of the flow and perpendicularly (Fig. 1). The tilt angle of the receiver tubes in the solar field ranges from −5° to 5°. [27] modeled the solar field thanks to ray tracing allowing to determine the concentrated solar flux received by the heliostat field (see Fig. 2). This flux distribution will be considered in the simulations to assess the non-homogeneity effect on the temperature field in the receiver.

Table 1
Solar field and power block specifications of the eLLO power plant. Available at [24].

Solar field	
Field aperture area [m^2]	153 000
Mirror width in line [m]	14
Number of lines	27
Mirror line length [m]	340
Power block	
Cycle capacity [MW]	9
Operating pressure [bar]	70
Cooling type	Dry

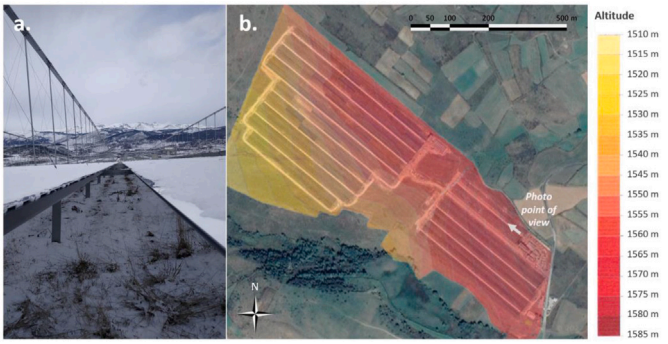

Fig. 1. Photo of eLLO's solar lines; b. topography of the site [27].

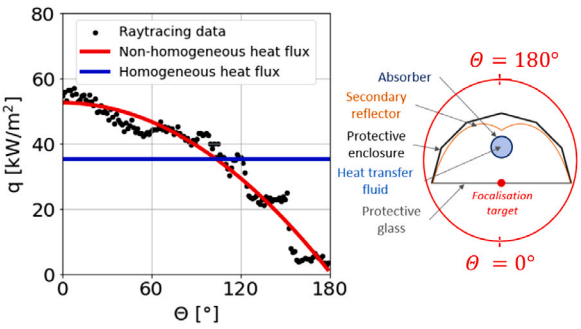

Fig. 2. Incident concentrated heat flux on the receivers of the eLLO power plant. The black points materialize the ray tracing simulations of [27] while the red curve represent a second degree polynomial fit (see Eq. (27)) of them. (For interpretation of the references to color in this figure legend, the reader is referred to the web version of this article.)

3. Numerical method

The numerical fluid dynamics simulations were conducted using version 7.0.2 of NEPTUNE_CFD. This software has been developed over several decades by French specialists in nuclear energy (EDF, CEA, IRSN and Framatome) and is among the most advanced tools for the numerical simulation of two-phase flows using the n-fluid approach. This approach is an extension of the two-fluid model by [28] to multiple

phases. It is a multiphase flow solver built upon the open-source software Code_Saturne.

NEPTUNE_CFD utilizes the Euler-Euler two-fluid model [29]. The governing equations within the software are discretized using a finite volume method with co-located variables. This technique solves the conservation equations of mass, momentum, and energy for each phase under a single pressure assumption. A second-order linear upwind scheme updates the volume fraction of each phase. The velocity field is computed using the SIMPLE algorithm [30]. To maintain the conservation of mass and energy, an iterative coupling method is applied to these equations [31]. The "alpha-pressure-energy cycle" algorithm used in Neptune CFD for solving flow is a pressure-based solver at first order in time. This means that the algorithm does not directly solve the Euler equations in their conservative form, but instead aims to achieve conservativity iteratively. This iterative approach allows for the coupling of velocity, pressure, and enthalpy to ensure consistency and guarantee an implicit resolution. This discretization scheme offers greater numerical robustness, efficiently manages fluid properties, and accurately models phase transitions. A coupled NEPTUNE_CFD/SYRTHES simulation was conducted to investigate the solid domain of the receiver. At each time step, SYRTHES calculates the temperature based on the heat flux applied to the outer surface of the tube. This temperature is then transmitted to NEPTUNE_CFD to compute the heat flux at the fluid–solid interface. This coupling method has been previously studied and validated in various applications where the accurate calculation of temperature within a solid domain is critically important [32–34]

3.1. Primary equations of the multi-regime Euler–Euler approach

For each cell, volume fractions α_k must satisfy the condition:

$$\sum_k \alpha_k = 1 \tag{1}$$

where $k \in [l, v]$ is the phase index.

The conservation of mass for the field k is expressed as:

$$\frac{\partial}{\partial t}\left(\alpha_k \rho_k\right) + \frac{\partial}{\partial x_i}\left(\alpha_k \rho_k u_{k,i}\right) = \sum_{p \neq k} \Gamma^c_{(p\to k)} + \Gamma^{nuc}_{(w,k)} \tag{2}$$

with $u_{k,i}$ the velocity component in the x_i direction, $\sum \Gamma^c_{(p\to k)}$ the mass transfer term at the interface from phase p to k given by Eq. (3), $\Gamma^{nuc}_{(w,k)}$ the mass term from wall-induced boiling to phase k.

$$\Gamma^c_{(p\to k)} = -\frac{\Pi'_{(p\to k)} + \Pi'_{(k\to p)}}{H^\sigma_{(p\to k)} - H^\sigma_{(k\to p)}} \tag{3}$$

with $\Pi'_{(p\to k)}$ the interfacial heat transfer independent of the mass transfer (calculated by the wall boiling model detailed in Section 3.2) and $H^\sigma_{(p\to k)}$ the enthalpy jump at the interface linked to the mass transfer.

The conservation of momentum for the field k is expressed :

$$\begin{aligned}\frac{\partial}{\partial t}(\alpha_k \rho_k \mathbf{u}_k) + \nabla\cdot(\alpha_k \rho_k \mathbf{u}_k \mathbf{u}_k) = -\alpha_k \nabla(P) + \alpha_k \rho_k \mathbf{g} \\ +\nabla\cdot\left(\alpha_k\left(\mu_k \mathbf{S}_k + \frac{S^T_k}{3}\mathbf{I}\right)\right) + \sum_{p\neq k}\mathbf{I}_{p\to k} + \alpha_k \mathbf{S}_c\end{aligned} \tag{4}$$

$\mathbf{I}_{p\to k}$ represents the momentum transfer term from phase p to k. The viscous stress $\mathbf{S}_k$ is given by Eq. (5).

$$\mathbf{S}_k = \frac{\partial \mathbf{u}_k}{\partial x_j} + \frac{\partial \mathbf{u}_k}{\partial x_i} - \frac{2}{3}\frac{\partial \mathbf{u}_k}{\partial x_i}\delta_{ij} \tag{5}$$

The momentum transfer at the interface depend on the flow topology. Originally, the method was developed for dispersed gaz liquid flow. In this case, the momentum transfer term reduces to the sum of a drag $\mathbf{M}^D_k$ [35], an added mass $\mathbf{M}^{AM}_k$ [36], a lift $\mathbf{M}^L_k$ [37,38] and a turbulent dispersion forces $\mathbf{M}^T_k$ [39] as depicted on Eq. (6).

$$\sum_{p\neq k}\mathbf{I}_{p\to k} = \mathbf{M}^D_k + \mathbf{M}^{AM}_k + \mathbf{M}^L_k + \mathbf{M}^T_k \tag{6}$$

Since fifteen years, a strong modeling effort [40–43] has been devoted to develop new closure law able to simulate cases involving multiple flow regimes. The main ingredients of such models consist of a detection algorithm, able to detect the interface type in the calculation domain, and specific closures, adapted to each flow regimes. For a detailed analysis of those models the reader is referred to the work of [44]. In our approach, bubbles smaller than the grid size, are considered as a dispersed gas phase (DG). For those structures Eq. (6) is considered. Larger bubbles and free surface flows, considered as continuous gas phase (CG), are modeled differently to enforce the normal velocity continuity at the interface and allow the latter to deform. To do so, one must consider a friction force $\mathbf{M}^F_k$ [40], a penalty force $\mathbf{M}^P_k$ [40] and a capillary force $\mathbf{M}^\sigma_k$ [45] as depicted on Eq. (7).

$$\sum_{p\neq k}\mathbf{I}_{p\to k} = \mathbf{M}^F_k + \mathbf{M}^P_k + \mathbf{M}^\sigma_k \tag{7}$$

The energy conservation is solved for the total enthalpy which leads to the formulation given by Eq. (8).

$$\begin{aligned}\frac{\partial}{\partial t}(\alpha_k \rho_k H_k) + \nabla\cdot(\alpha_k \rho_k H_k \mathbf{u}_k) = -\nabla\cdot(\alpha_k \mathbf{Q}_k) \\ + \alpha_k \frac{\partial P}{\partial t} + \alpha_k \rho_k \mathbf{g}\cdot\mathbf{u}_k + E^{int}_{p\to k}\end{aligned} \tag{8}$$

where $\mathbf{Q}_k = -\lambda_k \nabla T_k$, with λ_k as the thermal conductivity of phase k containing both molecular and turbulent contributions. P is the mean pressure and H_k is the total enthalpy of phase k, defined Eq. (9) and $E^{int}_{p\to k}$ the energy transfer term at the interface given by Eq. (10).

$$H_k = e_k + \frac{1}{2}u_k^2 + \frac{P}{\rho_k} \tag{9}$$

$$E^{int}_{p\to k} = \Gamma_{p\to k} H^\sigma_{p\to k} + \Pi'_{p\to k} \tag{10}$$

$\Gamma_{p\to k} H^\sigma_{p\to k}$ depends on mass transfer whereas $\Pi'_{p\to k}$ does not depend on the latter.

3.2. Wall boiling model

In the absence of wall boiling model dedicated to horizontal configuration at intermediate pressure levels in the literature, we used state of the art model implemented in the solver [46]. The model consists of two steps: the condition for boiling incipience and the heat flux calculation.

Hsu criterion is implemented to define the onset of boiling at the wall. It indicates that a bubble will grow in a vapor cavity if the liquid temperature, at the extremity of this cavity, is at least equal to the saturation temperature within the bubble [47]. Vapor is created inside a cavity if the radius is larger than the activation radius defined by:

$$r_{cl} = \frac{\lambda_s T_{crl}}{2\varphi_{wall}} \tag{11}$$

where T_{crl} is defined as the limit temperature below which there is no sustained boiling.

$$T_{crl} = \frac{8\sigma T_{sat}\varphi_{wall}}{H_{lat}\rho_{sat}\lambda_s}^{1/2} \tag{12}$$

Well-documented experimental study of [48] confirms the previous hypotheses. The boiling heat flux is splitted into three different terms: a single-phase flow convective heat flux q_c unaffected by the presence of bubbles, a quenching heat flux q_q and a vaporization heat flux q_e. Liquid convective heat transfer is written as:

$$q_c = A_c h_{\log}(T_w - T_l) \tag{13}$$

with T_w as the wall temperature and $h_{\log}$ the heat exchange coefficient. The heat flux due to quenching is given by:

$$q_q = A_b t_q f \frac{2\lambda_l (T_w - T_i)}{\sqrt{\pi a_l t_q}} \tag{14}$$

where A_b is the wall fraction occupied by bubble nucleation and $A_c = 1 - A_c$, f is the bubble detachment frequency, t_q is the quenching time and a_l is the liquid thermal diffusivity.

The bubble detachment diameter (d_d) is given by the correlation from [49]. The latter is valid for subcooled liquid but has been extended to saturated liquid. The bubble detachment diameter is given by:

$$d_d = 2.42 \times 10^{-5} P^{-0.709} \frac{a}{\sqrt{b\varphi}} \tag{15}$$

where P is the pressure and a, b and φ are parameters respectively given by Eqs. (16), (17), (19).

$$a = \frac{\left(T_w - T_{sat}\right)\lambda_s}{2\rho_v \ell \sqrt{\pi a_s}} \tag{16}$$

where λ_s and a_s denote the wall conductivity and thermal diffusivity, ρ_v denotes the vapor density and ℓ is the latent heat of vaporization.

$$b = \begin{cases} \frac{T_{sat} - T_l}{2(1-\rho_v/\rho_l)} & \text{if } St < 0.0065 \\ \frac{1}{2(1-\rho_v/\rho_l)} \frac{q_c + q_q + q_e}{0.0065 \rho_l C_{pl} |\mathbf{u}_l|} & \text{otherwise} \end{cases} \tag{17}$$

where $\|\mathbf{U}_l\|$ is the norm of the liquid velocity and St is the Stanton number which is defined by:

$$\mathrm{St} = \frac{q_c + q_q + q_e}{\rho_l C_{pl} \|\mathbf{U}_l\| \left(T_{sat} - T_l\right)} \tag{18}$$

$$\varphi = \max\left(1, \left(\frac{\|\mathbf{V}\|}{V_0}\right)^{0.47}\right), \text{ with } V_0 = 0.61\,\mathrm{m \cdot s^{-1}} \tag{19}$$

The quenching time and the bubble detachment frequency are modeled as proposed by [50]:

$$t_q = 1/f \tag{20}$$

$$f = \sqrt{\frac{4\, g\, |\rho_v - \rho_l|}{3 \rho_l d_d}} \tag{21}$$

The third heat flux density q_e used to model evaporation is given by:

$$q_e = f \frac{\pi d_d^3}{6} \rho_v \ell n \tag{22}$$

3.3. Turbulence modeling

The turbulence model chosen is the $R_{ij} - \varepsilon$ SSG model. Unlike the initial models proposed for single-phase flows ($k-\varepsilon$) for [51], the $R_{ij}-\varepsilon$ model is a second-order RANS model proposed by [52], in which each component of Reynolds stress tensor R_{ij} is solved as:

$$\begin{aligned} \frac{\partial R_{ij}}{\partial t} + v_k \frac{\partial R_{ij}}{\partial x_k} = &-R_{ik} \frac{\partial \bar{u}_j}{\partial x_k} - R_{jk} \frac{\partial \bar{u}_i}{\partial x_k} + \\ &- \Pi_{ij} + \frac{2}{3}\varepsilon \delta_{ij} + \mathcal{G}_{ij} \end{aligned} \tag{23}$$

where $P_{ij} = -R_{ik} \frac{\partial \bar{v}_j}{\partial x_k} - R_{jk} \frac{\partial \bar{v_i}}{\partial x_k}$ is the shear stress production term, Π_{ij} is the pressure-strain term, ε represents the scalar dissipation rate and $\mathcal{G}$ represents the gravity term. Similarly, advection/diffusion equation is solved for the dissipation ε:

$$\begin{aligned} \rho \frac{\partial \varepsilon}{\partial t} + \nabla \cdot (\rho \mathbf{u} \varepsilon - \mu \nabla \varepsilon) = &\, d_\varepsilon + C_{\varepsilon_1} \frac{\varepsilon}{k} \left(\mathcal{P} + \mathcal{G}_\varepsilon\right) \\ &- \rho C_{\varepsilon_2} \frac{\varepsilon^2}{k} + \varepsilon \nabla \cdot (\rho \underline{u}) \end{aligned} \tag{24}$$

where d_ε is the turbulent diffusion term, $\mathcal{P}$ is the shear stress production term and $\mathcal{G}_\varepsilon$ represents the gravity term for ε given by Eq. (25)

$$\mathcal{G}_\varepsilon = \max\left(0, \frac{1}{2} G_{kk}\right) \tag{25}$$

This turbulence model has been selected based on previous studies that have demonstrated the ability of this model to handle two-phase flows, where flow regime varies along the length [34].

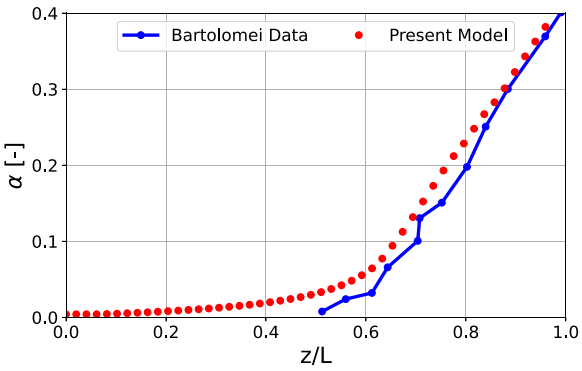

Fig. 3. Void fraction variation in the axial direction for the vertical boiling case of [53]. Comparison of our numerical results to the experimental data.

4. Model validation and mesh sensitivity analysis

4.1. Vertical boiling flow of Bartolomei

Our modeling approach has been validated using the experimental data obtained by [53]. The experiments were conducted with water in a vertical tube, of 15.4 mm inner diameter and 2 m length. The operating pressure is 45 bar, the mass flow rate is $G = 900\ \mathrm{kg \cdot m^{-2} \cdot s^{-1}}$, and a uniform heat flux $\dot{q} = 570\,\mathrm{kW \cdot m^2}$ is applied to the wall. Void fraction was determined by g-radiography. Signals were continuously recorded as the radiography unit was smoothly moved along the channel and provided void fraction measurements at any cross-section.

These data were chosen for validation because the experiments were conducted with water at high pressure, making them suitable for validating the present approach, especially the boiling model. The numerical results obtained for this case are confronted to the experimental data in Fig. 3. We observe a close match between the two evolutions, attesting the ability of our approach to model boiling flows.

4.2. DSG receiver of Pal & Kumar

Additionally, the approach is also confronted to horizontal boiling flow for which a stratified regime was numerically observed. DSG solar receiver simulations from [22] were selected as they consider the same physics. The selected case corresponds to a horizontal receiver with an inner diameter of 50 mm, an outer diameter of 70 mm, and a length of 12 m. The operating pressure is 30 bar, the mass flux is $G = 152\ \mathrm{kg \cdot m^{-2} \cdot s^{-1}}$, and a uniform heat flux of $\dot{q} = 15.74\,\mathrm{kW \cdot m^{-2}}$ is applied on the outer surface of the receiver. In their model, the authors consider the conjugated heat transfer between the receiver tube and the two phase flow inside. Fig. 4 shows the averaged void fraction along the length. A close match is observed between the two approaches as the discrepancies remains below 5%. Fig. 5 shows the comparison of the outer wall temperature profiles obtained with the two approaches for different streamwise positions. One can observe that our approach agrees well with the reference data. However, slight differences in wall bottom temperature are systematically observed. This might be due to water properties differences between the two softwares. The pressure drop along the domain was also assessed, in our simulations we calculated $\Delta P = 243.58$ Pa, while *Pal and Kumar* obtained $\Delta P_{\mathrm{Kumar}} = 221.85$ Pa. It represents a difference of 8.21%.

This comparison confirms the ability of our approach to model the horizontal boiling flows that occur in DSG solar receivers. Before describing our computational configuration, a detailed a mesh convergence study is presented.

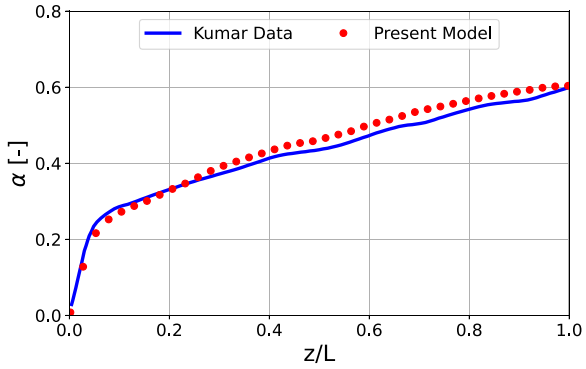

Fig. 4. Comparison of void fraction variation in the axial direction from numerical data recorded by [22].

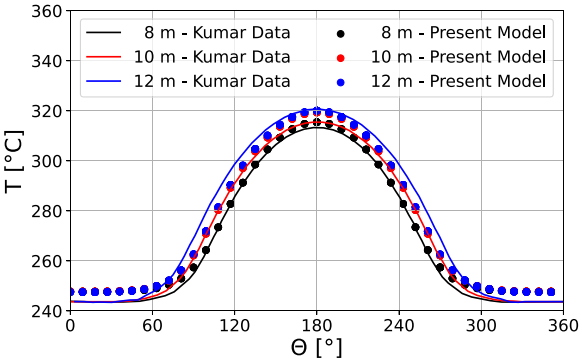

Fig. 5. Comparison of outer wall temperature from numerical data recorded by [22].

Table 2
Total number of cells per mesh. The cell number is given in thousands.

Streamwise	Elements per diameter			
asp. ratio	20	30	40	50
2	720	2321.4	5745.6	1154.4
4	360	1160.4	2872.8	5772
6	240	774	1915.2	3848
8	180	579.9	1436.4	2886

Table 3
Pressure drop for each case in Pa.

Streamwise	Elements per diameter			
asp. ratio	20	30	40	50
2	438.2	432.9	436.9	434.3
4	432.7	431.3	432.0	431.5
6	423.3	430.6	428.6	428.1
8	432.5	427.7	427.5	425.3

4.3. Mesh sensitivity analysis

To perform this mesh convergence study, both the number of cells per diameter and the aspect ratio of elements in the longitudinal direction are varied. The simulated case correspond to a 12 m long receiver operating at a pressure of 70 bar and with a mass flow rate $G = 304\ \mathrm{kg \cdot m^{-2} \cdot s^{-1}}$. The external homogeneous heat flux applied is $\dot{q} = 15.74\ \mathrm{kW \cdot m^{-2}}$. The different meshes employed are detailed in Table 2 with: the number of element per diameter, the aspect ratio in the streamwise direction and the resulting number of elements. A total of 16 simulations were performed. The pressure drop calculated for each mesh is presented in Table 3, indicating a maximum variation of 12 Pa between the different cases which is less than 3% variation. A second convergence indicator consists in calculating the root mean square (RMS) of the void fraction at the receiver outlet that was calculated for each case using Eq. (26). The results are shown in Fig. 6.

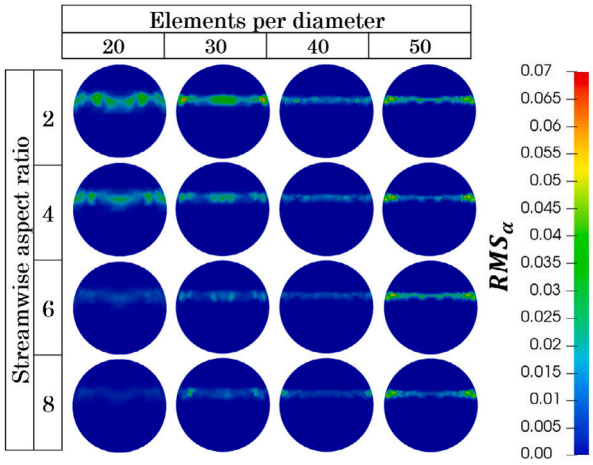

Fig. 6. Results for the mesh sensitivity analysis.

$$RMS_\alpha = \sqrt{\frac{1}{N}\sum_{i=1}^{N}(\alpha_i - \bar{\alpha})^2} \tag{26}$$

For this case, the two phase flow regime is stratified wavy. For such flow, the RMS_α is non-zero in cells crossed by the interface. The value of the indicator is directly linked to the ability of the mesh to capture the wave propagation on the interface. On Fig. 6, one can observe that, for meshes with less than 40 meshes per diameter, the contour of RMS_α gets blurry, meaning the resolution is not sufficient to properly capture the interface oscillation. This is in accordance with the work of [34]. A similar tendency is observed for meshes with high aspect ratio, the waves are poorly captured leading to a degradation of the subsequent temporal analyses. A fair trade-off between precision and mesh number — *ie* calculation cost — seems to be found for 40 meshes per diameter and an aspect ratio of 4. This mesh will then be used for the following simulations. Regarding the meshing in the solid part of the receiver, we have opted for 5 elements in the thickness of the tube, as previously done in similar studies by [22,34].

5. Numerical configurations and simulations procedure

5.1. Numerical set-up

In this study, we consider a 67 m long receiver, matching the dimensions of one of the modules of the eLLO power-plant. The inner diameter is 77.9 mm while the outer is 88.9 mm. The receiver is made of stainless steel whose thermophysical properties are detailed in Table 4. In the simulations, both uniform and non-uniform heat fluxes were applied to the outer surface of the receiver. The non-uniform heat flux was determined through Ray-Tracing simulations (see Fig. 2). Montanet et al. [27] concluded that the total concentrated incoming power does not vary by more than 1.4% with the tilt angle. For the sake of simplicity, it has been assumed in the following that concentrated incoming power remains the same whatever the tilt angle. Furthermore it does not depend on the streamwise direction. The simulation results were fitted with a second degree polynomial with respect to the circumferential coordinate ($0 < \Theta < 360$), to obtain Eq. (27). For the uniform heat flux case, the energy received from the non-uniform flux was integrated and divided by the surface area, yielding an equivalent uniform energy profile, depicted in Eq. (28).

$$\dot{q} = -0.0016\,\Theta^2 + 0.5734\,\Theta + 1.0311 \quad [\mathrm{kW \cdot m^{-2}}] \tag{27}$$

Table 4
Receiver material specifications [22].

Parameters	Value
Inner diameter	77.9 mm
Outer diameter	88.9 mm
Length	67 m
Density	8030 kg/m^3
Specific heat	503 J/kg K
Thermal conductivity	20 W/m K

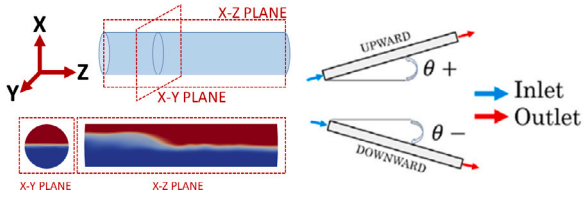

Fig. 7. Criteria for results and tilt.

$$\dot{q}_{\text{uniform}} = \frac{1}{360}\int_0^{360} \dot{q}(\Theta)\, d\Theta = 35.3 \quad [\text{kW}\cdot\text{m}^{-2}] \tag{28}$$

The boundary conditions considered for the case are as follows:

- **Inlet:** A constant mass flow of pure saturated liquid is imposed. Two mass flow were tested : $G = 300\ \text{kg}\cdot\text{m}^{-2}\cdot\text{s}^{-1}$ and $G = 600\ \text{kg}\cdot\text{m}^{-2}\cdot\text{s}^{-1}$.
- **Outlet:** A pressure condition is applied at the outlet and set at $P_{out} = 70$ bar which corresponds to the nominal operating pressure of the plant.
- **Inner wall:** No-slip walls are considered on the inner surface of the receiver, where the coupling between NEPTUNE_CFD and SYRTHES takes place.
- **Outer wall:** The previously mentioned uniform and non-uniform heat fluxes are applied.

The receiver tilt angle θ (see. Fig. 7) is adjusted throughout a volumetric force which allows to modify gravity as $g_x = -g\cos\theta$ and $g_z = -g\sin\theta$.

The working fluid is water. Its liquid and vapor physical properties are obtained from the CATHARE library integrated into the NEPTUNE_CFD code [54]. A detailed two-dimensional schematic model with boundary conditions is shown in Fig. 8. The geometry and meshing were generated using SALOME 9.6.0 software. Hexahedral elements were used for the fluid part, and tetrahedral elements for the receiver part, the latter being compatible with SYRTHES. The mesh was structured, oriented to keep the faces of the fluid part elements parallel to the interface position, thus minimizing numerical diffusion at the interface.

5.2. Simulation procedure

In this three-dimensional study of transient conjugate heat transfer, a total of 28 different simulations are conducted taking in account the whole domain without any symmetry plane. These simulations are performed to investigate the effects of mass flow rate, receiver tilt angle, and applied heat flux. Key aspects such as variation in void fraction, steam quality, steam outlet velocity, dynamic steam quality, and temperature distribution within the receiver are analyzed. Detailed analysis of the results is performed using the Paraview data postprocessing tool. The results are presented both as time-averaged values and in terms of temporal variability. A specific methodology has been followed to carry out the simulations, with the aim of optimizing computational resources, due to the number of simulated cases and

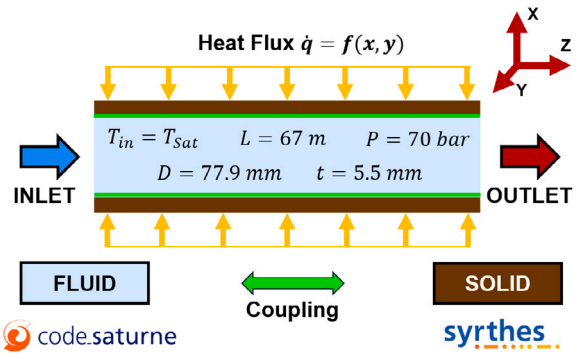

Fig. 8. 2D schematic diagram of the computational case.

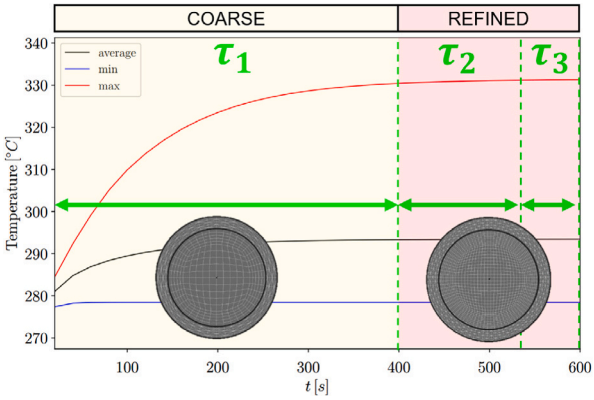

Fig. 9. Methodology followed in the simulation.

the size of the simulated domain. For this purpose, the simulation has been divided into three stages, which are chained one after the other by means of the option of resuming the simulation with a different mesh, available in the Neptune software. A first τ_1 time simulation is performed, starting from the receiver completely filled with liquid, on a coarse mesh. It allows to reach the desired quasi-steady state rapidly. Subsequently, the simulation is stopped and a time τ_2 is resumed with a refined mesh corresponding to the one selected in Section 4.3. This second stage aims to generate more accurate results, especially in the regions of the liquid-gas interface. Finally, the simulation is resumed again at time τ_3 where all the results are saved for further post-processing. Fig. 9 schematizes the methodology followed.

With respect to the temporal resolution of the simulation, an adaptive time-stepping approach has been employed. This methodology is particularly advantageous in simulations involving phase change at the interface, as the vapor phase generated can induce parasitic velocities. Ensuring an appropriate time step is crucial for maintaining the numerical stability of the simulation. To this end, the adaptative time step method ensures that the simulation time step never exceed the convective and diffusive stability timestep calculated for both phases.

6. Results and discussion

6.1. Tilt angle effect on void fraction, steam quality and flow pattern

Fig. 10 presents the evolution of the void fraction along the receiver length for various tilt angles, two different mass flow rate, $G = 300\ \text{kg}\cdot\text{m}^{-2}\cdot\text{s}^{-1}$ on Fig. 10(a) and $G = 600\ \text{kg}\cdot\text{m}^{-2}\cdot\text{s}^{-1}$ on Fig. 10(b), and a homogeneous heat flux distribution. It is evident that, whatever the tilt angle, the shape of the void fraction evolution slightly depends on the mass flow rate. Indeed, profiles are similar for both cases. However, for the smaller mass flow rate the void fraction is higher all along the

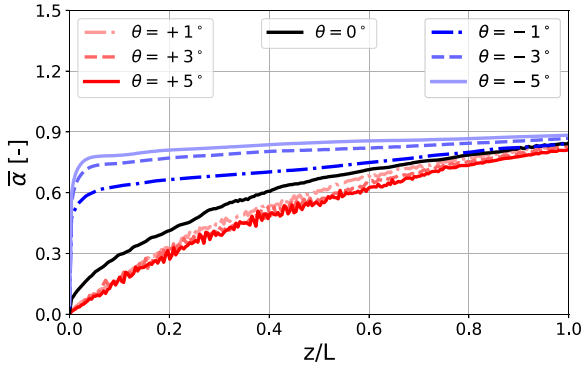

(a) G = 300 kg/(m²s)

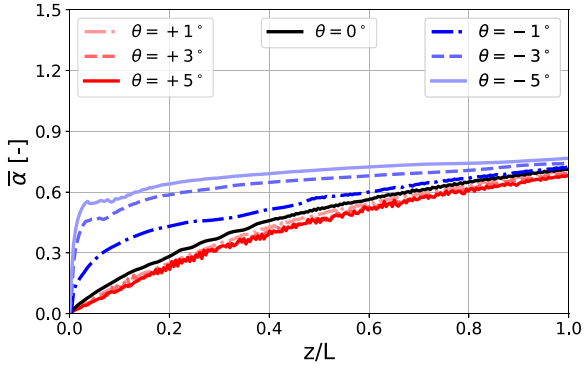

(b) G = 600 kg/(m²s)

Fig. 10. Void fraction versus dimensionless axial position.

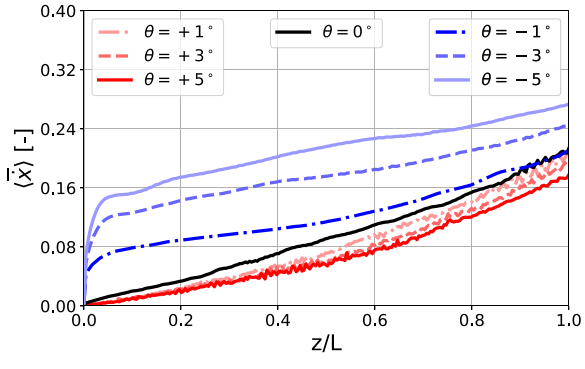

(a) G = 300 kg/(m²s)

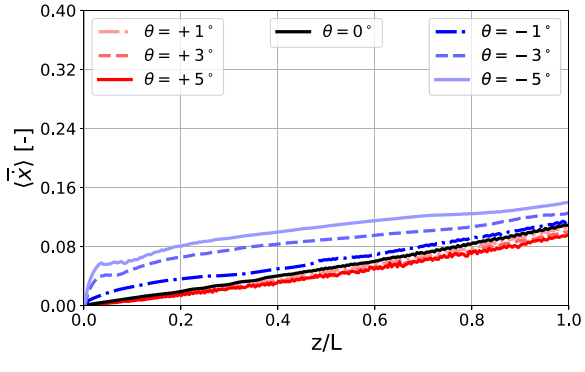

(b) G = 600 kg/(m²s)

Fig. 11. Steam quality versus dimensionless axial position.

receiver. At the outlet ($z/L = 1$), for the horizontal case, the void fraction reaches $\alpha_v = 0.85$ for the lower mass flow rate while it barely reaches $\alpha_v = 0.75$ for the higher one. This can be easily explained by an energy balance on the fluid flow. Furthermore, by comparison with the non-homogeneous flux case we observed the resulting void fraction evolution does not dependent on the applied heat flux distribution, owing to the redistribution effect of the solid wall, as depicted in Fig. 16. Regarding the influence of the tilt, Fig. 10 shows that for negative tilt angles, the steam travels towards the receiver inlet due to buoyancy effect, resulting in a rapid increase in void fraction at the inlet of the receiver. For positive angles, the volumetric fraction values tend to be lower, as the buoyancy force in this case acts in the streamwise direction and tends to evacuate the steam towards the outlet. For upward configurations, the evolution of α_v is noisier, reflecting the presence of a stratified wavy regime. In contrast, for descending configurations, the void fraction evolution flow is much more stable indicating a stably stratified regime.

Regarding steam quality, it has been computed according to Eq. (29):

$$\langle \bar{\dot{x}} \rangle = \frac{\langle \overline{\alpha \rho_v} \rangle}{\langle \overline{\alpha \rho_v} \rangle + \langle \overline{(1-\alpha)\rho_l} \rangle} \tag{29}$$

where ρ_l and ρ_v correspond respectively to liquid and steam densities. As there is no significant variation of the properties along the receiver length, similar trends to those observed for void fractions are obtained in Fig. 11. It can be generally concluded that negative tilt angles favor steam production. Indeed, in such cases, the buoyancy effects tend to increase the residence time of the steam in the receiver, leading to a rise in overall steam production.

To visualize the flow patterns inside the receiver, the temporal fluctuation of the void fraction has been computed using Eq. (26). As discussed before, Fig. 12 shows that for negative tilt angles, owing to a stably stratified regime, no temporal oscillations of the void fraction are observed. Whereas for positive tilt angles, a stratified-wavy regime is observed. This flow pattern arises when void fractions are below $\alpha = 0.5$ and steam phase velocities are high, and tend to trigger shear instabilities forming waves (as observed experimentally in [6]). The occurrence of larger oscillations in the flow pattern has been observed previously by Odeh [55]. He reported that tilting the receiver caused the flow pattern to transition to intermittent flow which is undesirable in plant operation due to the large massflow and pressure fluctuations associated to this flow pattern. Fig. 13 shows that the streamwise steam velocity is higher for positive tilt angles. For $x/L = 0.2$, whatever the mass flow rate, it is clear that the streamwise velocity is roughly twice faster for $\theta = 5°$ than for $\theta = -5°$. Finally, it is apparent that for all the simulated cases, no intermittent flow pattern — where the receiver cross section is sometimes filled with liquid water — is observed. From an operational standpoint, this outcome is favorable, as such a flow pattern complicates the operation of the solar plant.

6.2. Tilt angle effect on the streamwise steam velocity and dynamic quality

Fig. 12 shows different contour plot in the XZ planes after a geometrical adjustment required to display the entire domain for such a high aspect ratio geometry. In the center plot, the region occupied by the liquid phase is shaded in black and color map indicates the magnitude of the streamwise component of the steam velocity. It can be noted that for negative tilt angles the appearance of negative velocity indicating the presence of steam recirculation towards the inlet. Such recirculation is observed, whatever the mass flows and the heat flux distribution, for all negative tilt angle simulations. The latter is driven by the buoyancy force acting on the vapor phase. This backward circulation results in a region with axial velocity close to zero for negative tilt angles. The opposite effect is also observed for positive tilt angles, the buoyancy force aids evacuating the steam towards the outlet, resulting in steam acceleration and higher outlet velocities. Fig. 12 depicts that for a mass

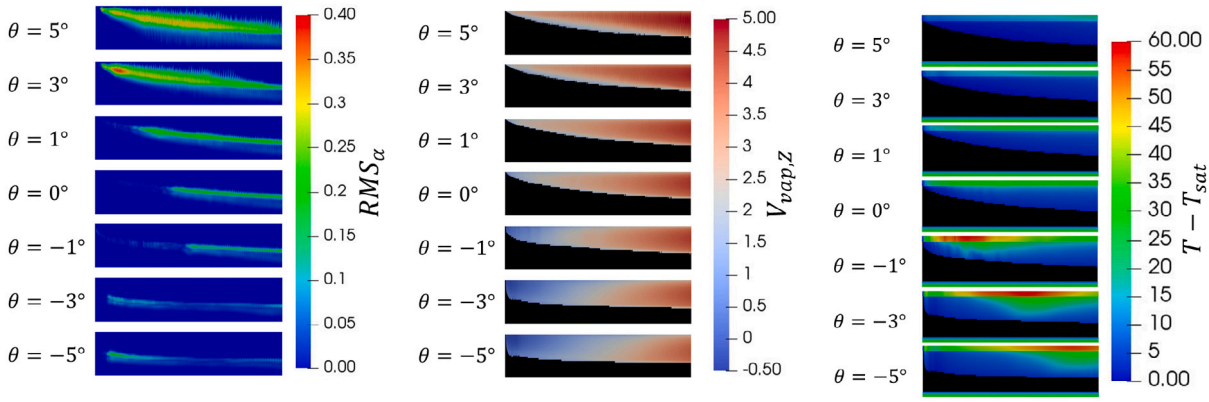

Fig. 12. XZ planes of RMS of void fraction (left), time averaged steam velocity (center) and time averaged steam and tube temperature (right) for non-homogeneous heat flux and $G = 600\ \mathrm{kg \cdot m^{-2} \cdot s^{-1}}$.

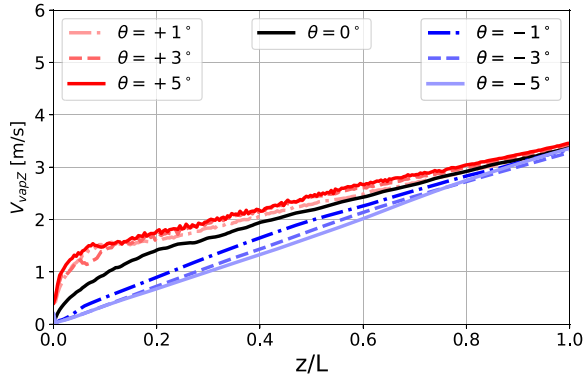

(a) G = 300 kg/(m²s)

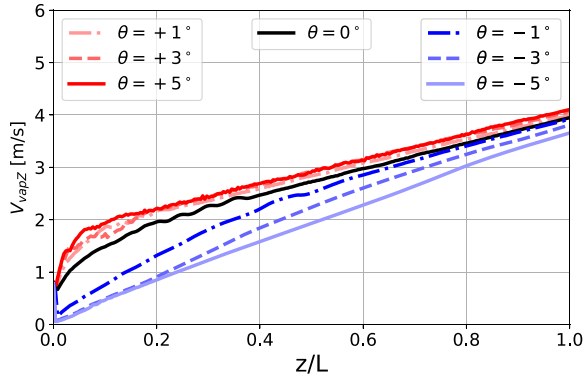

(b) G = 600 kg/(m²s)

Fig. 13. Steam streamwise velocity versus dimensionless axial position for a non homogeneous heat flux distribution.

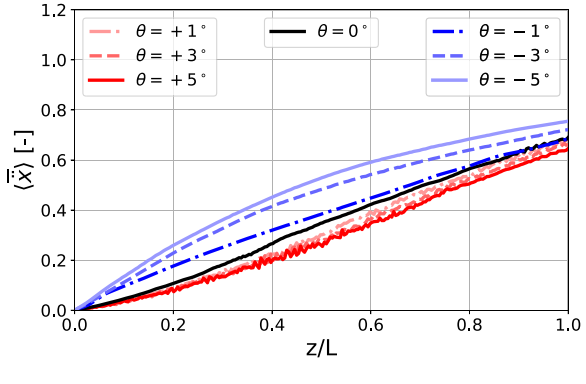

(a) G = 300 kg/(m²s)

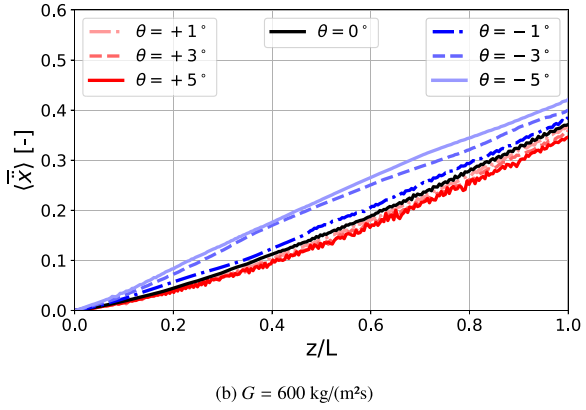

(b) G = 600 kg/(m²s)

Fig. 14. Dynamic quality versus dimensionless axial position.

flow of $G = 600\ \mathrm{kg \cdot m^{-2} \cdot s^{-1}}$, the steam velocity at the outlet locally reaches up to $v_v = 5$ m/s.

The cross section averaged streamwise steam velocity evolution along the receiver is depicted in Fig. 13. For negative tilt angles, the steam velocities near the inlet are lower than the imposed inlet velocities of the case, respectively $v_{in} = 0.41\ \mathrm{m \cdot s^{-1}}$ for $G = 300\ \mathrm{kg \cdot m^{-2} \cdot s^{-1}}$ and $v_{in} = 0.82\ \mathrm{m \cdot s^{-1}}$ for $G = 600\ \mathrm{kg \cdot m^{-2} \cdot s^{-1}}$. This is directly related to the recirculation observed on Fig. 12 and provides an indication of its influence. For a positive tilt, two regions can be distinguish on the average velocity curve. A first region in which the vapor accelerates rapidly following a logarithmic law, which stabilizes around $z/L = 0.1$ (resp. $z/L = 0.2$) for $G = 300\ \mathrm{kg \cdot m^{-2} \cdot s^{-1}}$ (resp. $G = 600\ \mathrm{kg \cdot m^{-2} \cdot s^{-1}}$). In the second region, the flow linearly accelerates until the receiver outlet.

A similar trend is observed for the dynamic steam quality — calculated with Eq. (30) (where v_l and v_v correspond respectively to liquid and steam velocities) and shown in Fig. 14 — where values are higher for negative tilt angles than for positive ones.

$$\langle \bar{\dot{x}} \rangle = \frac{\langle \overline{\alpha \rho_v v_v} \rangle}{\langle \overline{\alpha \rho_v v_v} \rangle + \langle \overline{(1-\alpha) \rho_l v_l} \rangle} \tag{30}$$

6.3. Tilt angle effect on steam and solid temperature

The right part of Fig. 12 shows temperature excess ($T - T_{sat}$) contours of in the XZ-plane (see Fig. 7) of both the vapor and the solid phase for

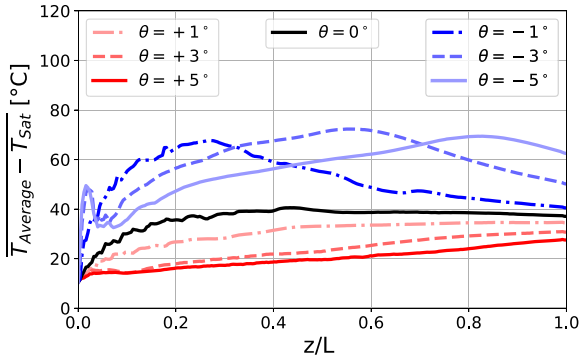

(a) Homogeneous heat flux.

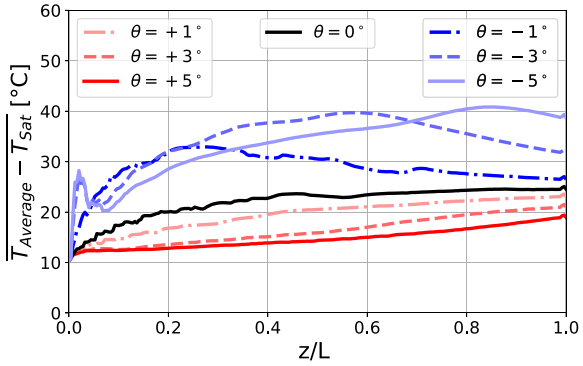

(b) Non-Homogeneous heat flux.

Fig. 15. Average cross section tube temperature versus dimensionless axial position for $G = 600$ kg/(m^{2}s).

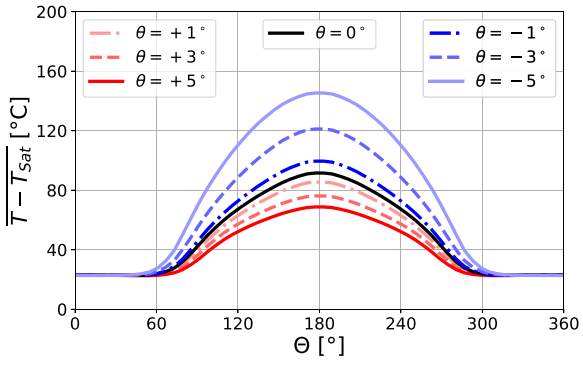

(a) Homogeneous heat flux.

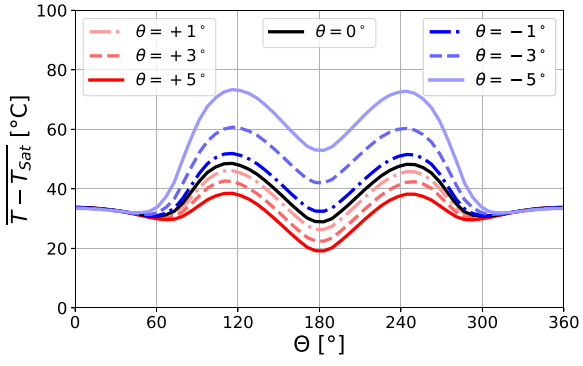

(b) Non-Homogeneous heat flux.

Fig. 16. Outer wall tube temperature versus circumferential position for $G = 600$ kg/(m^{2}s).

a non homogeneous flux distribution and $G = 600\ \text{kg} \cdot \text{m}^{-2} \cdot \text{s}^{-1}$. For positive tilt angles, the temperature excess in the steam phase remains always below 10 K highlighting a relative homogeneity. In the receiver, no hot spot is visible and the temperature excess does not exceed 40 K. Both quantities linearly increase in the streamwise direction. Whereas, for negative tilt angles, both the steam and receiver temperature highlight strong non-homogeneous spatial variation. Analysis reveals that the maximum peak temperature location of both the steam and the receiver, appear at a streamwise upper location depending on the tilt angle. Decreasing the tilt angle results in the hot spot moving closer to the inlet. Such displacement of the hot spot can also be seen in Fig. 15 which displays the cross section averaged of the temperature excess in the receiver with respect to the length, for $G = 600\ \text{kg}\cdot\text{m}^{-2}\cdot\text{s}^{-1}$ and both heat flux distributions. The trends are similar for both flux distribution but the peak temperature reach systematically higher values for the homogeneous distribution, for example for $\theta = -5°$ it reaches 70 K for the homogeneous distribution against 40 K for the non-homogeneous one. In the case of stratified flow, the upper portion of the receiver is exclusively exposed to vapor. When a homogeneous flux distribution is applied, the heat flux in the upper region is excessively high to be effectively dissipated by the vapor flow, resulting in an increase in the temperature of the solid. Additionally, for positive and zero tilt angles the temperature excess evolution is monotonous with respect to the length. The more negative the tilt angles the smaller the temperature excess.

Finally, Fig. 16 compares the external receiver temperature distribution at the outlet ($x/L = 1$) for both flux distributions. It is observable that for the homogeneous one, the temperature excess maximum appears at the top of the receiver — owing to both the thermal boundary condition and the low heat transfer coefficient of the vapor phase in contact with the upper part of the receiver. It becomes clear on Fig. 16(b) that the temperature distribution is strongly affected by the heat flux distribution. For the non-homogeneous flux, the temperature excess peak is no longer at the top but shifts by about 60° — owing to the coupling between the Θ distribution of the heat flux and the ability of the flow to efficiently evacuate the heat. For both flux distribution, the tilt angle effects on the temperature excess is similar. For downward flows, the temperature excess increases with the tilt while it decreases for upward flows. Fig. 17 shows, for $G = 600\ \text{kg} \cdot \text{m}^{-2} \cdot \text{s}^{-1}$ and the non-homogeneous flux distribution, temperature excess contour at four different streamwise position and for all tilt angles. The temperature profile obtained are consistent with the analysis proposed for Figs. 15(b) and 16(b).

7. Summary and concluding remarks

In this study, we evaluated the tilt angle and the concentrated solar heat flux distribution effects on flow regimes and temperature distribution in a DSG solar receiver. To this end, a non-stationary three-dimensional model taking into account conjugate heat transfer has been set up coupling NEPTUNE_CFD and SYRTHES software. The approach has been validated by comparison to relevant cases from the literature. A mesh convergence analysis allowed to identify a mesh yielding a satisfactory trade-off between precision and calculation cost. Simulations reproduce a 67 m long module of the eLLO power plant. Two mass flow rates, $G = 300\ \text{kg} \cdot \text{m}^{-2} \cdot \text{s}^{-1}$ and $G = 600\ \text{kg} \cdot \text{m}^{-2} \cdot \text{s}^{-1}$, eleven tilt angles, ranging from −5° to 5° and two different flux distributions were simulated. The main findings are summarized below.

1. **Heat flux distribution effect:** Homogeneous heat flux leads to higher section averaged receiver temperature than the non-homogeneous distribution. The maximum moves towards the inlet for angles close to horizontal and towards the outlet for more negative angles, indicating significant temperature gradients. In a cross section, the homogeneous heat flux generates a single receiver temperature maximum at the top of the receiver

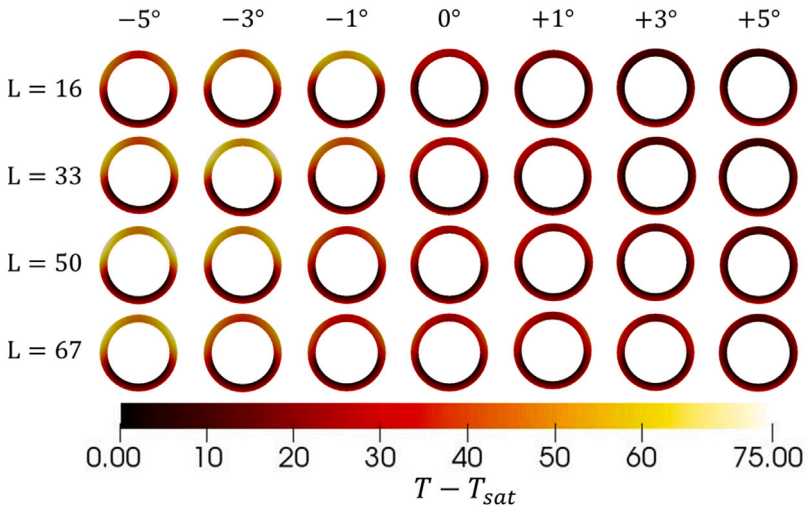

Fig. 17. Results for fluid and solid part for non-homogeneous heat flux and $G = 600$ kg/(m^{2}s).

while a non-uniform distribution leads to two maxima shifted by 60° from the top. The boundary condition strongly influences the temperature distribution in the receiver, but does not affect the total amount of steam produced. This conclusion can be useful when pre-dimensioning a solar receiver, since it states that the exact flux distribution is not required to pre-dimension the line length to reach the targeted steam quality at the receiver's outlet.

2. **Mass Flow Rate effect:** The void fraction increases with a decrease of the mass flow rate due to longer fluid residence time in the receiver. For lower mass flow, the receiver temperature maximum is reached closer to the inlet and has a higher magnitude.
3. **Tilt angle effect on flow patterns:** Tilt angle significantly influences phase distribution in the receiver. Negative angles increase void fraction near the inlet due to buoyancy-driven recirculation, while positive angles reduce it by aiding steam evacuation. Positive tilts enhance steam evacuation and outlet velocities, promoting shear instabilities and stratified-wavy flow. In contrast, negative tilts lead to stably stratified flow with steam recirculating toward the inlet, reducing steam streamwise velocity. Steam quality trends follow these patterns, with higher dynamic steam quality at negative angles, but increasing near the outlet for positive tilts at lower mass flow rates. Our results highlight that although the amount of steam produced is slightly higher for negative tilt angles, the receiver temperature reached levels that might compromise its integrity. Such tilts configuration must thus be avoided. Furthermore, although a slight positive tilt promotes a stratified wavy flow, it significantly decreases the receivers's temperature in operation which might increase the receiver lifespan.
4. **Design and Operational Implications:** These findings are critical for optimizing solar plant receivers. Avoiding intermittent flow patterns is vital for stable operation, as constant fluid contact with the receiver's surface is necessary to prevent operational complications. Simulations highlight that downward flows promote steam production but generate stronger temperature gradient in the receiver which may generate stronger thermal stress and fatigue.

The present study investigates the influence of tilt angle and boundary conditions on the nominal operating parameters of the eLLO solar plant, as summarized in the previous conclusions. Although pressure is a variable that directly affects the thermophysical properties of the fluid, the results indicate that flow regimes are primarily influenced by gravitational effects for such horizontal flow configuration.

Future improvements to this work should include a broader exploration of operating parameters and transient phenomena, such as the effect of cloud transients on the dynamics of steam generation within the receiver. These conclusions underscore the importance of considering mass flow rate, tilt angle, and heat flux distribution when designing and operating solar receiver systems to optimize thermal performance and enhance durability. Future efforts will focus on developing an experimental database for horizontal and slightly tilted boiling flow applicable to this technology.

CRediT authorship contribution statement

Israël Aguilera-Cortes: Writing – original draft, Validation, Software, Project administration, Methodology, Funding acquisition, Formal analysis, Data curation, Conceptualization. **Adrien Toutant:** Writing – review & editing, Visualization, Supervision, Conceptualization. **Samuel Mer:** Writing – review & editing, Visualization, Supervision, Project administration, Funding acquisition, Conceptualization.

Declaration of competing interest

The authors declare that they have no known competing financial interests or personal relationships that could have appeared to influence the work reported in this paper.

Acknowledgments

This work was funded by the European Union as part of the TOPCSP project (HORIZON MSCA Doctoral Network, Project number 101072537). This project was provided with computer and storage resources by GENCI at IDRIS thanks to the grant 2023-A0152B14649 on the CSL partition of the supercomputer Jean Zay. Finally, the authors would like to thank Florent Lecat (eLLO), Nicolas Merigoux (EDF), Hervé Neau (IMFT) and Maxime Pigou (IMFT) for their technical support.

References

[1] H.M. Müller-Steinhagen, F. Trieb, Concentrating solar power, — A review of the technology, 2004, URL https://api.semanticscholar.org/CorpusID:106949393.

[2] M. Biencinto, L. González, L. Valenzuela, A quasi-dynamic simulation model for direct steam generation in parabolic troughs using TRNSYS, Appl. Energy 161 (2016) 133–142, http://dx.doi.org/10.1016/j.apenergy.2015.10.001, URL https://linkinghub.elsevier.com/retrieve/pii/S0306261915012283.

[3] A. Fernández-García, E. Zarza, L. Valenzuela, M. Pérez, Parabolic-trough solar collectors and their applications, Renew. Sustain. Energy Rev. 14 (7) (2010) 1695–1721, http://dx.doi.org/10.1016/j.rser.2010.03.012, URL https://linkinghub.elsevier.com/retrieve/pii/S1364032110000675.

[4] Y. Taitel, A.E. Dukler, A model for predicting flow regime transitions in horizontal and near horizontal gas–liquid flow, AIChE J. 22 (1) (1976) 47–55, http://dx.doi.org/10.1002/aic.690220105, URL https://aiche.onlinelibrary.wiley.com/doi/10.1002/aic.690220105.

[5] N. Kattan, J.R. Thome, D. Favrat, Flow boiling in horizontal tubes: Part 1—Development of a diabatic two-phase flow pattern map, J. Heat Transfer 120 (1) (1998) 140–147, http://dx.doi.org/10.1115/1.2830037, URL https://asmedigitalcollection.asme.org/heattransfer/article/120/1/140/383031/Flow-Boiling-in-Horizontal-Tubes-Part-1Development.

[6] L. Wojtan, T. Ursenbacher, J.R. Thome, Investigation of flow boiling in horizontal tubes: Part II—Development of a new heat transfer model for stratified-wavy, dryout and mist flow regimes, Int. J. Heat Mass Transfer 48 (14) (2005) 2970–2985, http://dx.doi.org/10.1016/j.ijheatmasstransfer.2004.12.013, URL https://linkinghub.elsevier.com/retrieve/pii/S001793100500027X.

[7] O. Baker, Design of pipelines for the simultaneous flow of oil and gas, in: SPE Annual Technical Conference and Exhibition?, SPE, 1953, pp. SPE–323.

[8] J.M. Mandhane, G.A. Gregory, K. Aziz, A flow pattern map for gas—liquid flow in horizontal pipes, Int. J. Multiph. Flow 1 (4) (1974) 537–553, http://dx.doi.org/10.1016/0301-9322(74)90006-8, URL https://linkinghub.elsevier.com/retrieve/pii/0301932274900068.

[9] R. Cundapí, S.L. Moya, L. Valenzuela, Approaches to modelling a solar field for direct generation of industrial steam, Renew. Energy 103 (2017) 666–681, http://dx.doi.org/10.1016/j.renene.2016.10.081, URL https://linkinghub.elsevier.com/retrieve/pii/S0960148116309582.

[10] S.D. Odeh, Direct Steam Generation Collectors for Solar Electric Generation Systems (Ph.D. thesis), UNSW Sydney, 1999.

[11] M. Eck, W. Steinmann, Dynamic behavior of the direct solar steam generation in parabolic trough collectors: A simulation study, in: Proc, of 10th Solar PACES Int. Symp. on Solar Thermal Concentrating Technologies, 2000, pp. 101–106.

[12] W.-D. Steinmann, Dynamik Solarer Dampferzeuger (Ph.D. thesis), Universität Stuttgart, 2001.

[13] R. Silva, M. Pérez, A. Fernández-Garcia, Modeling and Co-simulation of a parabolic trough solar plant for industrial process heat, Appl. Energy 106 (2013) 287–300.

[14] L. Valenzuela, D. Hernández-Lobón, E. Zarza, M. Pérez, Pressure losses in small-sized parabolic-trough solar fields for industrial process heat, in: ISES Solar World Congress. Kassel, Germany, 2011.

[15] M. Ishii, K. Mishima, Two-fluid model and hydrodynamic constitutive relations, Nucl. Eng. Des. 82 (2–3) (1984) 107–126, http://dx.doi.org/10.1016/0029-5493(84)90207-3, URL https://linkinghub.elsevier.com/retrieve/pii/0029549384902073.

[16] M.I. Roldán, L. Valenzuela, E. Zarza, Thermal analysis of solar receiver pipes with superheated steam, Appl. Energy 103 (2013) 73–84, http://dx.doi.org/10.1016/j.apenergy.2012.10.021, URL https://linkinghub.elsevier.com/retrieve/pii/S0306261912007271.

[17] J.J. Serrano-Aguilera, L. Valenzuela, L. Parras, Thermal 3D model for direct solar steam generation under superheated conditions, Appl. Energy 132 (2014) 370–382, http://dx.doi.org/10.1016/j.apenergy.2014.07.035, URL https://linkinghub.elsevier.com/retrieve/pii/S030626191400717X.

[18] E. Zarza, L. Valenzuela, J. Leo'n, H.-D. Weyers, M. Eickhoff, M. Eck, K. Hennecke, The DISS project: Direct steam generation in parabolic trough systems. Operation and maintenance experience and update on project status, J. Sol. Energy Eng. 124 (2) (2002) 126–133, http://dx.doi.org/10.1115/1.1467645, URL https://asmedigitalcollection.asme.org/solarenergyengineering/article/124/2/126/461459/The-DISS-Project-Direct-Steam-Generation-in.

[19] E. Zarza, L. Valenzuela, J. León, K. Hennecke, M. Eck, H.-D. Weyers, M. Eickhoff, Direct steam generation in parabolic troughs: Final results and conclusions of the DISS project, Energy 29 (5–6) (2004) 635–644, http://dx.doi.org/10.1016/S0360-5442(03)00172-5, URL https://linkinghub.elsevier.com/retrieve/pii/S0360544203001725.

[20] M. Eck, W.-D. Steinmann, J. Rheinländer, Maximum temperature difference in horizontal and tilted absorber pipes with direct steam generation, Energy 29 (5–6) (2004) 665–676, http://dx.doi.org/10.1016/S0360-5442(03)00175-0, URL https://linkinghub.elsevier.com/retrieve/pii/S0360544203001750.

[21] O.E. Itabiyi, THE effect of tilt angle and mass flow rate on the performance of a parabolic trough solar concentrator via experimentation, Adv. Phys. Theor. Appl. (2024) http://dx.doi.org/10.7176/APTA/88-01, URL https://iiste.org/Journals/index.php/APTA/article/view/62130.

[22] R.K. Pal, R.K. K, Thermo-hydrodynamic modeling of flow boiling through the horizontal tube using Eulerian two-fluid modeling approach, Int. J. Heat Mass Transfer 168 (2021) 120794, http://dx.doi.org/10.1016/j.ijheatmasstransfer.2020.120794, URL https://linkinghub.elsevier.com/retrieve/pii/S0017931020337327.

[23] R.K. Pal, R.K. K, Two-fluid modeling of direct steam generation in the receiver of parabolic trough solar collector with non-uniform heat flux, Energy 226 (2021) 120308, http://dx.doi.org/10.1016/j.energy.2021.120308, URL https://linkinghub.elsevier.com/retrieve/pii/S0360544221005570.

[24] eLLO solar thermal project CSP project, URL https://solarpaces.nrel.gov/project/ello-solar-thermal-project.

[25] M. Ploquin, S. Mer, A. Toutant, F. Roget, CFD investigation of level fluctuations in steam accumulators as thermal storage: A direct steam generation application, Sol. Energy 245 (2022) 11–18, http://dx.doi.org/10.1016/j.solener.2022.08.048, URL https://linkinghub.elsevier.com/retrieve/pii/S0038092X22005977.

[26] J. Muñoz-Antón, R. Abbas, J. Martínez-Val, M. Montes, Going further with Fresnel receiver: New design window for direct steam generation, Energy Procedia 49 (2014) 184–192, http://dx.doi.org/10.1016/j.egypro.2014.03.020, URL https://linkinghub.elsevier.com/retrieve/pii/S1876610214004743.

[27] E. Montanet, S. Rodat, Q. Falcoz, F. Roget, Influence of topography on the optical performances of a Fresnel linear asymmetrical concentrator array: The case of the eLLO solar power plant, Energy 274 (2023) 127310, http://dx.doi.org/10.1016/j.energy.2023.127310, URL https://linkinghub.elsevier.com/retrieve/pii/S0360544223007041.

[28] T. Hibiki, M. Ishii, One-dimensional drift-flux model and constitutive equations for relative motion between phases in various two-phase flow regimes, Int. J. Heat Mass Transfer 46 (25) (2003) 4935–4948, http://dx.doi.org/10.1016/S0017-9310(03)00322-3, URL https://linkinghub.elsevier.com/retrieve/pii/S0017931003003223.

[29] M. Ishii, T. Hibiki, Connection to other statistical averages, in: Thermo-Fluid Dynamics of Two-Phase Flow, Springer New York, New York, NY, 2011, pp. 119–128, http://dx.doi.org/10.1007/978-1-4419-7985-8_6, URL https://link.springer.com/10.1007/978-1-4419-7985-8_6.

[30] S.V. Patankar, D.B. Spalding, A calculation procedure for heat, mass and momentum transfer in three-dimensional parabolic flows, Int. J. Heat Mass Transfer 15 (10) (1972) 1787–1806, http://dx.doi.org/10.1016/0017-9310(72)90054-3, URL https://linkinghub.elsevier.com/retrieve/pii/0017931072900543.

[31] S. Mimouni, M. Boucker, J. Laviéville, A. Guelfi, D. Bestion, Modelling and computation of cavitation and boiling bubbly flows with the NEPTUNE_CFD code, Nucl. Eng. Des. 238 (3) (2008) 680–692, http://dx.doi.org/10.1016/j.nucengdes.2007.02.052, URL https://linkinghub.elsevier.com/retrieve/pii/S0029549307003494.

[32] J.P. Mañes, V.H. Sánchez Espinoza, S. Chiva Vicent, M. Böttcher, R. Stieglitz, Validation of NEPTUNE-CFD two-phase flow models using experimental data, Sci. Technol. Nucl. Install. 2014 (2014) 1–19, http://dx.doi.org/10.1155/2014/185950, URL http://www.hindawi.com/journals/stni/2014/185950/.

[33] N. Mérigoux, J. Laviéville, S. Mimouni, M. Guingo, C. Baudry, S. Bellet, Verification, validation and application of NEPTUNE_CFD to two-phase pressurized thermal shocks, Nucl. Eng. Des. 312 (2017) 74–85, http://dx.doi.org/10.1016/j.nucengdes.2016.06.041, URL https://linkinghub.elsevier.com/retrieve/pii/S0029549316302023.

[34] E. Butaye, A. Toutant, S. Mer, Euler–Euler multi-scale simulations of internal boiling flow with conjugated heat transfer, Appl. Mech. 4 (1) (2023) 191–209, http://dx.doi.org/10.3390/applmech4010011, URL https://www.mdpi.com/2673-3161/4/1/11.

[35] M. Ishii, N. Zuber, Drag coefficient and relative velocity in bubbly, droplet or particulate flows, AIChE J. 25 (5) (1979) 843–855, http://dx.doi.org/10.1002/aic.690250513, URL https://aiche.onlinelibrary.wiley.com/doi/10.1002/aic.690250513.

[36] N. Zuber, On the dispersed two-phase flow in the laminar flow regime, Chem. Eng. Sci. 19 (11) (1964) 897–917, http://dx.doi.org/10.1016/0009-2509(64)85067-3, URL https://linkinghub.elsevier.com/retrieve/pii/0009250964850673.

[37] A. Tomiyama, H. Tamai, I. Zun, S. Hosokawa, Transverse migration of single bubbles in simple shear flows, Chem. Eng. Sci. 57 (11) (2002) 1849–1858, http://dx.doi.org/10.1016/S0009-2509(02)00085-4, URL https://linkinghub.elsevier.com/retrieve/pii/S0009250902000854.

[38] R.M. Wellek, A.K. Agrawal, A.H.P. Skelland, Shape of liquid drops moving in liquid media, AIChE J. 12 (5) (1966) 854–862, http://dx.doi.org/10.1002/aic.690120506, URL https://aiche.onlinelibrary.wiley.com/doi/10.1002/aic.690120506.

[39] M. Lance, M.L. De Bertodano, Phase distribution phenomena and wall effects in bubbly two-phase flows, Multiph. Sci. Technol. 8 (1–4) (1994) 69–123, http://dx.doi.org/10.1615/MultScienTechn.v8.i1-4.30, URL http://www.dl.begellhouse.com/journals/5af8c23d50e0a883,2d2fda127764a47f,1e6b5eaa78073157.html.

[40] P. Coste, A large interface model for two-phase CFD, Nucl. Eng. Des. 255 (2013) 38–50, http://dx.doi.org/10.1016/j.nucengdes.2012.10.008, URL https://linkinghub.elsevier.com/retrieve/pii/S0029549312005213.

[41] R. Denèfle, S. Mimouni, J.-P. Caltagirone, S. Vincent, Multifield hybrid approach for two-phase flow modeling — Part 1: Adiabatic flows, Comput. & Fluids 113 (2015) 106–111, http://dx.doi.org/10.1016/j.compfluid.2014.07.018.

[42] N. Merigoux, J. Lavieville, S. Mimouni, M. Guingo, C. Baudry, A generalized large interface to dispersed bubbly flow approach to model two-phase flows in nuclear power plant, in: CFD4NRS-6, Cambridge, MA - USA, Paper 11-1, 2016, pp. 1–20.

[43] S. Fleau, Multifield Approach and Interface Locating Method for Two-Phase Flows in Nuclear Power Plant (Ph.D. thesis), Univ. Paris Est Marne-La-Vallée, France, 2017.

[44] S. Mer, O. Praud, H. Neau, N. Merigoux, J. Magnaudet, V. Roig, The emptying of a bottle as a test case for assessing interfacial momentum exchange models for Euler–Euler simulations of multi-scale gas-liquid flows, Int. J. Multiph. Flow 106 (2018) 109–124, http://dx.doi.org/10.1016/j.ijmultiphaseflow.2018.05.002, URL https://linkinghub.elsevier.com/retrieve/pii/S0301932218301472.

[45] J.U. Brackbill, D.B. Kothe, C. Zemach, A continuum method for modeling surface tension, J. Comput. Phys. 100 (2) (1992) 335–354, http://dx.doi.org/10.1016/0021-9991(92)90240-Y, URL https://linkinghub.elsevier.com/retrieve/pii/002199919290240Y.

[46] N. Kurul, M.Z. Podowski, Multidimensional effects in forced convection subcooled boiling, in: Proceeding of International Heat Transfer Conference 9, Begellhouse, Jerusalem, Israel, 1990, pp. 21–26, http://dx.doi.org/10.1615/IHTC9.40, URL http://ihtcdigitallibrary.com/conferences/6ec9fdc764f29109,3b6668e93c4d03e5,1968e4d71e4e45b1.html.

[47] Y.Y. Hsu, On the size range of active nucleation cavities on a heating surface, J. Heat Transfer 84 (3) (1962) 207–213, http://dx.doi.org/10.1115/1.3684339, URL https://asmedigitalcollection.asme.org/heattransfer/article/84/3/207/430157/On-the-Size-Range-of-Active-Nucleation-Cavities-on.

[48] R. Hino, T. Ueda, Studies on heat transfer and flow characteristics in subcooled flow boiling—Part 1. Boiling characteristics, Int. J. Multiph. Flow 11 (3) (1985) 269–281, http://dx.doi.org/10.1016/0301-9322(85)90058-8, URL https://linkinghub.elsevier.com/retrieve/pii/0301932285900588.

[49] H.C. Ünal, Maximum bubble diameter, maximum bubble-growth time and bubble-growth rate during the subcooled nucleate flow boiling of water up to 17.7 MN/m2, Int. J. Heat Mass Transfer 19 (6) (1976) 643–649, http://dx.doi.org/10.1016/0017-9310(76)90047-8, URL https://linkinghub.elsevier.com/retrieve/pii/0017931076900478.

[50] R. Cole, A photographic study of pool boiling in the region of the critical heat flux, AIChE J. 6 (4) (1960) 533–538, http://dx.doi.org/10.1002/aic.690060405, URL https://aiche.onlinelibrary.wiley.com/doi/10.1002/aic.690060405.

[51] B.E. Launder, D.B. Spalding, The numerical computation of turbulent flows, Comput. Methods Appl. Mech. Engrg. 3 (2) (1974) 269–289, http://dx.doi.org/10.1016/0045-7825(74)90029-2, URL https://linkinghub.elsevier.com/retrieve/pii/0045782574900292.

[52] C.G. Speziale, S. Sarkar, T.B. Gatski, Modelling the pressure–strain correlation of turbulence: An invariant dynamical systems approach, J. Fluid Mech. 227 (1991) 245–272, http://dx.doi.org/10.1017/S0022112091000101, URL https://www.cambridge.org/core/product/identifier/S0022112091000101/type/journal_article.

[53] G.G. Bartolomei, V.G. Brantov, Y.S. Molochnikov, Y.V. Kharitonov, V.A. Solodkii, G.N. Batashova, V.N. Mikhailov, An experimental investigation of true volumetric vapor content with subcooled boiling in tubes, Therm. Eng. 29 (3) (1982) 132–135.

[54] P. Emonot, A. Souyri, J. Gandrille, F. Barré, CATHARE-3: A new system code for thermal-hydraulics in the context of the NEPTUNE project, Nucl. Eng. Des. (2011) S0029549311004018, http://dx.doi.org/10.1016/j.nucengdes.2011.04.049, URL https://linkinghub.elsevier.com/retrieve/pii/S0029549311004018.

[55] S.D. Odeh, M. Behnia, G.L. Morrison, Hydrodynamic analysis of direct steam generation solar collectors, J. Sol. Energy Eng. 122 (1) (2000) 14–22.